AIP | Journal of Applied Physics

Full-quantum simulation of hole transport and band-to-band tunneling in nanowires using the kp method

Mincheol Shin

Citation: J. Appl. Phys. 106, 054505 (2009); doi: 10.1063/1.3208067
View online: http://dx.doi.org/10.1063/1.3208067
View Table of Contents: http://jap.aip.org/resource/1/JAPIAU/v106/i5
Published by the American Institute of Physics.

Additional information on J. Appl. Phys.

Journal Homepage: http://jap.aip.org/
Journal Information: http://jap.aip.org/about/about_the_journal
Top downloads: http://jap.aip.org/features/most_downloaded
Information for Authors: http://jap.aip.org/authors

ADVERTISEMENT

Downloaded 19 Apr 2013 to 143.248.118.125. This article is copyrighted as indicated in the abstract. Reuse of AIP content is subject to the terms at: http://jap.aip.org/about/rights_and_permissions

JOURNAL OF APPLIED PHYSICS 106, 054505 (2009)

Full-quantum simulation of hole transport and band-to-band tunneling in nanowires using the $k\cdot p$ method

Mincheol Shin[a)]
Department of Electrical Engineering, KAIST, Daejeon 305-701, Republic of Korea

(Received 29 April 2009; accepted 20 July 2009; published online 3 September 2009; publisher error corrected 4 September 2009)

We have developed a three-dimensional, self-consistent full-quantum transport simulator for nanowire field effect transistors based on the eight-band $k\cdot p$ method. We have constructed the mode-space Hamiltonian via a unitary transformation from the Hamiltonian discretized in the k-space, and reduced its size significantly by selecting only the modes that contribute to the transport. We have also devised an approximate but highly accurate method to solve the cross-sectional eigenvalue problems, thereby overcoming the numerical bottleneck of the mode-space approach. We have therefore been able to develop a highly efficient device simulator. We demonstrate the capability of our simulator by calculating the hole transport in a p-type Si nanowire field effect transistor and the band-to-band tunneling current in a InAs nanowire tunnel field effect transistor. © *2009 American Institute of Physics*. [doi:10.1063/1.3208067]

I. INTRODUCTION

The short channel effects (SCEs) of conventional planar metal oxide semiconductor field effect transistors (MOSFETs) are major obstacles in downsizing of the devices into the nanometer scale regime. As a candidate for next-generation devices that can significantly reduce SCE and possibly replace the conventional MOSFETs, nanowire FETs with multiple gates have drawn considerable attention and have been subject of active researches in recent years.[1,2]

In the modeling and simulation of electrical properties of such nanowire devices, transport should be treated fully quantum mechanically, and self-consistent charge densities and potential profile should be obtained by solving the Schrödinger equation together with the Poisson's equation. Simulators based on the single-band effective-mass Hamiltonian have been developed to simulate nanowire FETs with n-type channel,[3–5] and it has been verified, against more rigorous, atomistic tight-binding (TB)-based simulators, that they are valid down to about 3×3 nm^2 cross sections.[6,7] The single-band effective-mass Hamiltonian can be, however, no longer applied to devices where valence bands are involved, such as Si p-type FETs and III-V MOSFETs with band-to-band tunneling (BTBT) effect because the heavy and light holes in valence band are strongly coupled to each other and so they cannot be described by an effective-mass Hamiltonian which gives simple parabolic dispersion relationship.

The $k\cdot p$ (KP) method is one of the most popular methods to describe the valence band of Si and both conduction and valence bands of direct band gap semiconductors.[8] It has been widely applied to the problem of calculating electronic structures of various semiconductors. The transport problems, semiclassical or quantum mechanical, have been also addressed by using KP, although the full quantum treatment has been mostly restricted to one-dimensional transport problems.[9] Recently, a quantum transport simulation of a ultrathin body (UTB) device using KP has been demonstrated, but it was non-self-consistent calculation based on the four-band Hamiltonian, and the focus of the work was rather to demonstrate the capability of the contact block reduction method.[10]

The TB method is another widely used method to describe valence bands. Recently, full-quantum, self-consistent transport simulators based on TB have been developed and successfully applied to UTB and nanowire FETs[11,12] but the computational burden of the simulators is enormous. The TB model is generally regarded more accurate than the KP model, mainly due to its atomistic treatment. In self-consistent transport simulations of FETs with a few hundred millivolts of drain bias applied, however, the difference between the two models is expected to be diminished.

In this work, we have applied the $k\cdot p$ method to the three-dimensional (3D), self-consistent, and full-quantum transport problem in nanowire devices. To the best of our knowledge, there has been no such previous attempt. We were able to develop a computationally highly efficient simulator by reducing the size of the Hamiltonian via transformation to the mode-space basis and resolving the issue of solving eigenvalue problems for each cross-sectional plane, which is a numerically challenging problem common to all mode-space approaches. Hence, compared to TB-based full-quantum simulators, our KP simulator has clear advantage in terms of the computational cost. In this paper, we will focus on the theory, numerical aspect, and capability of our KP simulator. The benchmarking of the TB and KP approaches will be deferred to later publication, where it will be shown that the results from the two approaches agree quite well.

II. APPROACH

A. The KP Hamiltonian and its discretization

A schematic diagram of the 3D nanowire FET considered in this work is shown in Fig. 1. The source and drain are

a)Electronic mail: mshin@kaist.ac.kr.

 © 2009 American Institute of Physics

Downloaded 19 Apr 2013 to 143.248.118.125. This article is copyrighted as indicated in the abstract. Reuse of AIP content is subject to the terms at: http://jap.aip.org/about/rights_and_permissions

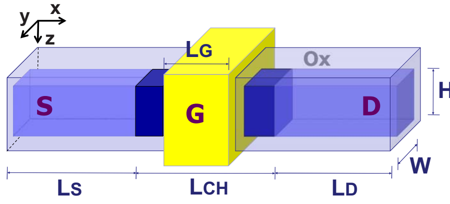

FIG. 1. (Color online) Schematic diagram of the nanowire field effect transistor considered in this work. The channel and gate length, L_{ch} and L_{G} can be, in general, different, but in this work $L_{\mathrm{ch}}=L_{\mathrm{C}}$. L_{S} and L_{D} are source and drain length, respectively, and H and W are channel height and width, respectively.

heavily n or p doped semi-infinite semiconducting wires, the channel is usually intrinsic or lightly doped, and the gates surround the channel as shown in the figure. To simulate the transport in the device, we have used a 8×8 KP Hamiltonian that is written as

$$H_{\mathrm{KP}}(k_x,k_y,k_z)=H_{0,\mathrm{KP}}(k_x,k_y,k_z)+V_{\mathrm{KP}}, \tag{1}$$

where $H_{0,\mathrm{KP}}(k_x,k_y,k_z)$ and V_{KP} are given by Eqs. (A2)–(A15). To construct the Hamiltonian matrix suitable for numerical calculation, we first discretize $H_{\mathrm{KP}}(k_x,k_y,k_z)$ in the real space, by converting $k_v\to -i\partial/\partial v$, where $v=x,y,z$. The discretized Hamiltonian in the real space is then of the form

$$\mathcal{H}_R=\begin{bmatrix} H_R(1) & W_R & & & \\ W_R^\dagger & H_R(2) & W_R & & \\ & W_R^\dagger & H_R(3) & & \\ & & & \ddots & W_R \\ & & & W_R^\dagger & H_R(N_x) \end{bmatrix}, \tag{2}$$

where N_x is the number of cross-sectional planes in the transport (x) direction. The Hamiltonian $H_R(i)$ for the ith plane and the coupling Hamiltonian W_R are $N_bN_R\times N_bN_R$ matrices, where N_b is the number of bands used in the KP Hamiltonian ($N_b=8$ for the eight band KP Hamiltonian) and $N_R=N_yN_z$, where N_y and N_z are numbers of real space grid points in the y and z directions, respectively. $H_R(i)$ can be written as

$$H_R(i)=H_{0R}+V_R(i), \tag{3}$$

where H_{0R} is the discretized kinetic Hamiltonian of Eq. (A2) and $V_R(i)$ is a diagonal matrix with diagonal elements corresponding to the potential $E_{C(V)}-q_0\phi(x_i,y,z)$ in the ith plane, where $E_{C(V)}$ is the conduction (valence) band edge, $\phi(x,y,z)$ is the vacuum level potential, and q_0 is the elementary charge.

The Hamiltonian $\mathcal{H}_R$ in Eq. (2) discretized in the real space can be transformed to k-space via a unitary transformation as follows:

$$\mathcal{H}_K=\mathcal{U}_K^\dagger\mathcal{H}_R\mathcal{U}_K, \tag{4}$$

where $\mathcal{U}_K$ is a unitary matrix given in Eq. (B2). $\mathcal{H}_K$ is written as

$$\mathcal{H}_K=\begin{bmatrix} H_K(1) & W_K & & & \\ W_K^\dagger & H_K(2) & W_K & & \\ & W_K^\dagger & H_K(3) & & \\ & & & \ddots & W_K \\ & & & W_K^\dagger & H_K(N_x) \end{bmatrix}, \tag{5}$$

where

$$H_K(i)=U_K^\dagger H_R(i)U_K=H_{0K}+V_K(i), \tag{6}$$

$$W_K=U_K^\dagger W_R U_K. \tag{7}$$

where

$$H_{0K}\equiv U_K^\dagger H_{0R}U_K \tag{8}$$

and

$$V_K(i)\equiv U_K^\dagger V_R(i)U_K. \tag{9}$$

See Appendix B for detailed description of the k-space transformation.

The advantage of using the k-space Hamiltonian lies in that, using a simple reordering scheme as detailed in Appendix C, we can elect to use smaller-sized Hamiltonian. That is, the size N_bN_K of discretized k-space Hamiltonians can be much smaller than the size of its counterpart in the real space which is N_bN_R. N_K depends on the cross-sectional area of a nanowire and also on the energy range near a band edge that one is interested in. For instance, if one desires to accurately produce a subband structure of a Si nanowire of 5×5 nm^2 in the energy range of 0.5 eV from the valence band edge, $N_K=200$ would be sufficient, while N_K should be bigger if one wishes to consider a wider energy range. A typical size N_R in the real space is 2500 for the nanowire of the same dimension. The k-space Hamiltonian can be therefore effectively reduced in size to less than one-tenth of its real-space counterpart.

B. Mode-space Hamiltonian

For an efficient full-quantum simulation, the k-space Hamiltonian turned out to be still too big to handle. We have therefore employed a mode-space approach where much smaller-sized mode-space Hamiltonian can be used. We first define "mode" in the ith cross-sectional plane as follows:

$$[H_K(i)+W_K+W_K^\dagger]|\psi_m(i)\rangle=E_m(i)|\psi_m(i)\rangle, \tag{10}$$

where the mth eigenfunction $|\psi_m(i)\rangle$ represents the mth mode. We then form a unitary matrix that consists of the mode wave functions as column vectors,

Downloaded 19 Apr 2013 to 143.248.118.125. This article is copyrighted as indicated in the abstract. Reuse of AIP content is subject to the terms at: http://jap.aip.org/about/rights_and_permissions

$$U_M(i) = (|\psi_1(i)\rangle|\psi_2(i)\rangle \cdots |\psi_{N_M}(i)\rangle), \tag{11}$$

where N_M is the number of modes that we select. We transform the original Hamiltonian via

$$\mathcal{H}_M \equiv \mathcal{U}_M^\dagger \mathcal{H}_K \mathcal{U}_M, \tag{12}$$

where

$$\mathcal{U}_M = \begin{bmatrix} U_M(1) & & & & \\ & U_M(2) & & & \\ & & U_M(3) & & \\ & & & \ddots & \\ & & & & U_M(N_x) \end{bmatrix}. \tag{13}$$

Then,

$$\mathcal{H}_M = \begin{bmatrix} H_M(1) & W_M(1) & & & \\ W_M^\dagger(1) & H_M(2) & W_M(2) & & \\ & W_M^\dagger(2) & H_M(3) & & \\ & & & \ddots & W_M(N_x-1) \\ & & & W_M^\dagger(N_x-1) & H_M(N_x) \end{bmatrix}, \tag{14}$$

where

$$H_M(i) = U_M^\dagger(i) H_K U_M(i), \tag{15}$$

$$W_M(i) = U_M^\dagger(i) W_K U_M(i+1). \tag{16}$$

If the unitary matrix $U_M(i)$ of the ith cross-section consists of N_M mode wavefunctions, i.e., if $U_M(i)$ is a $N_bN_K \times N_M$ matrix, the Hamiltonian $\mathcal{H}_M$ becomes a $N_xN_M \times N_xN_M$ matrix.

C. Cross-section eigenvalue problems

Solving the eigenvalue problem in Eq. (10) for each cross-sectional plane is demanding computationally, even if we use the reduced-sized k-space Hamiltonian instead of much bigger real-space Hamiltonian. We have therefore devised a highly efficient way to solve the eigenvalue problem as follows. Let us first define

$$h_0 \equiv H_{0K} + W_K + W_K^\dagger \tag{17}$$

and $\bar{U}$ as the $N_bN_K \times N_M$ unitary matrix which diagonalizes h_0,

$$\bar{U}^\dagger h_0 \bar{U} = \bar{D}, \tag{18}$$

where $\bar{D}$ is a $N_M \times N_M$ diagonal matrix. Recall that H_{0K} is the kinetic part of the Hamiltonian so h_0 is independent of potential. In the ith plane, we should solve the eigenvalue problem for

$$h(i) \equiv H_K(i) + W_K + W_K^\dagger = h_0 + V_K(i), \tag{19}$$

that is,

$$U_M^\dagger(i) h(i) U_M(i) = D(i), \tag{20}$$

where $U_M(i)$ and $D(i)$ are the unitary matrices diagonalizing $h(i)$ and the resultant diagonal matrix, respectively. Instead of directly diagonalizing $h(i)$, we make a unitary transformation as follows:

$$\tilde{h}(i) \equiv \bar{U}^\dagger h(i) \bar{U} = \bar{D} + \bar{U}^\dagger V_K(i) \bar{U}, \tag{21}$$

and we diagonalize the transformed matrix $\tilde{h}(i)$. *As an excellent approximation*, we diagonalize only the first $N_M \times N_M$ submatrix of $\tilde{h}(i)$ instead of the full matrix. That is, the problem now becomes finding N_M eigenvectors from $N_M \times N_M$ submatrix, instead of from $N_bN_K \times N_bN_K$ full matrix. Let us denote as $U_r(i)$ the $N_M \times N_M$ unitary matrix that diagonalizes the submatrix. Then,

$$U_M(i) = \bar{U} U_r(i). \tag{22}$$

The computation cost is therefore reduced by a factor proportional to $(N_bN_K/N_M)^r$, where r is usually around 2.7 (the number depends on the numerical algorithm that one uses). Since N_M and N_bN_K in this work are typically 200 and 8×200, respectively, a huge computational save can be achieved. We note that, if a single-band parabolic effective-mass (PEM) Hamiltonian is used instead of the multiband KP Hamiltonian, the method described in this section is reduced to the project-space method for solving cross-sectional Schrödinger equations for electrons.[13]

D. Selection of modes

The transformation matrix $\bar{U}$ in Eqs. (17) and (18) consists of N_M column vectors (=modes) which are wavefunctions at $k=0$ of the nanowire dispersion relationship. For an efficient simulation, N_M should be as small as possible, without losing accuracy in simulation at the same time. We therefore focused on the energy range of a few tenth of 1 eV from the band edges where most of the charge transport takes place and selected modes that are contained in the energy range as follows.

We note that for a single-band PEM Hamiltonian, a mode can be assigned to each subband. For the KP Hamiltonian, however, it is not possible because wavefunctions at different k in the same subband are, in general, different. In terms of the modes defined in this work, it means that a

Downloaded 19 Apr 2013 to 143.248.118.125. This article is copyrighted as indicated in the abstract. Reuse of AIP content is subject to the terms at: http://jap.aip.org/about/rights_and_permissions

subband contains many modes; that is, we can expand the wave function $|\psi_n(k)\rangle$ at k in the nth subband in terms of the mode wave functions $|\psi_m\rangle$ as

$$|\psi_n(k)\rangle = \sum_m a_{nm}(k)|\psi_m\rangle, \tag{23}$$

and, by calculating the magnitude of the coefficient $a_{nm}(k) = \langle\psi_m|\psi_n(k)\rangle$, we can identify the modes that constitutes the particular subband. By inspecting the modes that are contained in the subbands within the energy range of interest, we select modes to be used for the matrix $\bar{U}$, and using the relationship in Eq. (22), we determine the mode transformation matrix $U_M(i)$ for each cross section. In this way, one can avoid choosing modes one after another starting from the first mode, in which case a larger number of modes would be needed.

We note that our mode-space approach becomes equivalent to the so-called coupled mode-space approach when applied to n-type Si FETs using a single-band PEM Hamiltonian[3] and carbon nanotube FETs using a single-band TB Hamiltonian.[14] The so-called uncoupled mode-space approach where modes are treated as independent does not correctly produce subband structures and is not relevant to our work here. Although our mode-space Hamiltonian is much reduced in its size from the full Hamiltonian, it retains all the features of the latter in the energy range we are interested in, as will be discussed shortly in Sec. III A.

E. Simulation details

We have employed the nonequilibrium Green's function approach to solve the quantum ballistic transport problem formulated in the mode space. At the start of the simulation, we select the mode wavefunctions from the k-space Hamiltonian and construct the unitary matrix $\bar{U}$ of Eq. (18) as described above. These steps are performed only once, even when a voltage sweep is performed. Using the transformation matrix in Eq. (22), the mode-space Hamiltonian of Eq. (14) is constructed and fed into the procedure to obtain the retarded Green's functions. See Fig. 2. In this work, the recursive Green's function (RGF) method[15] was used and the contact self-energies were calculated using the method in Ref. 16. In the electrostatic part, the 3D Poisson's equation with the following convergence scheme was solved,

$$\nabla^2\phi^k = -\frac{q}{\epsilon}(N_D + p_{3D}^k e^{-(\phi^k-\phi^{k-1})/k_BT} - n_{3D}^k e^{(\phi^k-\phi^{k-1})/k_BT}), \tag{24}$$

where ϕ^k, p_{3D}^k, and n_{3D}^k are the kth self-consistent-step solutions for the potential, hole density, and electron density, respectively, and N_D is the doping profile. The fixed-value boundary condition for the Poisson's equation was used for the gate contact region and the free boundary condition was used for other boundaries including source/drain contacts. After the self-consistent potential was obtained, the current was calculated.

Note that we have performed the mode-space transformation from the k-space Hamiltonian. This has apparent disadvantage of having to perform $U_K^\dagger V_R(i) U_K$ to transform the

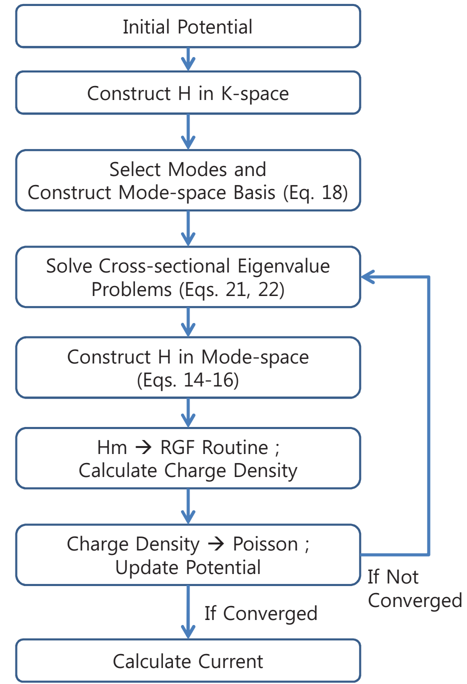

FIG. 2. (Color online) Flowchart of the simulation.

real-space potential to k-space and to construct $U_K U_M(i)$ for transformation back to the real space. Overall, however, the transformation from the k-space Hamiltonian is much more efficient than the direct transformation from the real space Hamiltonian because the matrix multiplications in Eqs. (15) and (16), in particular, significantly slow down the numerical performance if the much bigger-sized real-space Hamiltonian is used.

Since our simulator is based on the mode-space approach, its numerical efficiency is strongly dependent on the number of modes being used. Table I shows an example of measured wall time in one self-consistent cycle using a 32-node, 3.0 GHz Intel cluster. It can be seen in the table that total wall time increases as $N_M{}^\gamma$ where $\gamma \sim 2.3$. The number of modes being used is usually in the range of 100–200, depending on the device type and its cross-sectional size: for a Si nanowire pMOSFET with 5×5 nm^2 channel cross sec-

TABLE I. Measured wall time in one self-consistent cycle using a 32-node, 3.0 GHz Intel cluster as a function of the number of modes (N_M). Numbers are in units of seconds. The sample device for the wall-time measurement is a Si nanowire PMOSFET with 5×5 nm^2 channel cross section and 30 nm device length and the 6×6 $k\cdot p$ Hamiltonian was used. The number of energy points in the RGF routine was 16 per node, which is usually enough for our nonuniform, adaptive energy-grid scheme.

	N_M			
Routines	90	120	180	240
Cross-sectional eigenvalue problem	1.6	2.5	4.6	7.2
Mode-space Hamiltonian construction	16.7	26.1	53.6	91.0
RGF	27.5	61.4	193	430
Transformation back to real space	3.6	6.0	18.4	27.3
Poisson equation	8.8	8.8	8.8	8.8
Total	58	105	278	564

Downloaded 19 Apr 2013 to 143.248.118.125. This article is copyrighted as indicated in the abstract. Reuse of AIP content is subject to the terms at: http://jap.aip.org/about/rights_and_permissions

tion and 30 nm device length, for instance, a gate-voltage sweep with ten bias points can be finished in 5 h (wall time) using the above-mentioned cluster.

III. RESULTS

A. Examination of the mode-space approach

In this section, we compare our mode-space solutions against the full Hamiltonian solutions and show that our mode-space approach correctly produces the desired results, despite that the size of the mode-space Hamiltonian is much smaller than that of the full Hamiltonian. We first would like to mention why this verification of our mode-space approach is necessary. For a single-band PEM Hamiltonian applied to electrons in the conduction band, the use of the mode-space Hamiltonian makes sense physically and can be well justified, and 10–20 coupled or uncoupled modes are sufficient for a nanowire of 5×5 nm^2 cross section. For the KP Hamiltonian applied to holes in the valence band, however, the use of the mode-space approach as formulated in Sec. II is not as obvious because the "modes" as we have defined in this work rather correspond to the "choice of basis functions" than to "subbands." As previously pointed out, the concept of modes and subbands are identical in the PEM case for electrons, but they are not in the KP case for holes. Therefore, we need to check whether our mode-space approach, which is in essence to use only a subset from a complete basis set, works indeed. We mean by our mode-space approach that the approximate method to solve the cross-sectional eigenvalue problems described in Sec. II is also included. In the following, we will demonstrate the comparison between the mode-space and full Hamiltonian solutions in three stages: we will first compare the valence subbands produced by the both methods and then do the same for transmission in a BTBT situation. We will finally compare the current-voltage characteristics. What we mean by the "full solution" is that we use the full k-space Hamiltonian in Eq. (5) which is directly fed to the RGF procedure; the mode-space transformation is not performed and hence solving the cross-sectional eigenvalue problems is not needed.

We first compare the nanowire subband structures generated by using the mode-space Hamiltonian and by using the full Hamiltonian. As it should be, the subband structure from the mode-space Hamiltonian becomes closer to that from the full Hamiltonian as the number of modes being used is increased, as can be seen in Fig. 3 where the valence-band subband structures of Si [100] nanowire of 5×5 nm^2 square cross section are shown. One can see in the figure that with $N_m=120$, the subband profile produced by the mode-space approach is quite close in shape to that from the full solution, although there is some difference in detail. With $N_m=240$, the two subband profiles are very close to each other. We note that the subband structures shown in Fig. 3 are the ones obtained after tuning the KP parameters so that the subband structures from KP and TB agree closely. The KP parameters used are $\gamma_1=3.55$, $\gamma_2=0.65$, $\gamma_3=1.26$, and $\Delta_{SO}=0.044$. Details of such tuning will be published elsewhere.

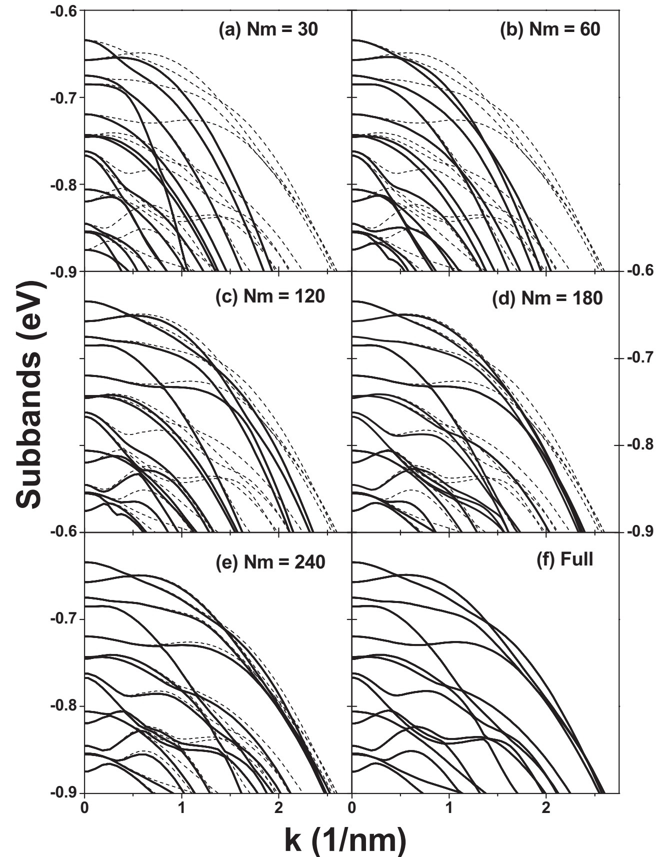

FIG. 3. Valence subband structures of a Si [100] nanowire of 5×5 nm^2 cross section using the mode-space Hamiltonian with (a) 30, (b) 60, (c) 120, (d) 180, and (e) 240 modes and (f) the full k-space Hamiltonian. In (a)–(e), the full-Hamiltonian subbands are overlaid (dashed lines). The energy is referenced to the Si midgap (0.56eV from the bulk valence-band edge).

We next compare the transmission calculated from using the mode-space Hamiltonian and from using the full Hamiltonian. In Fig. 4, the transmission $T(E)$ in a BTBT condition as a function of energy E is shown for an InAs nanowire

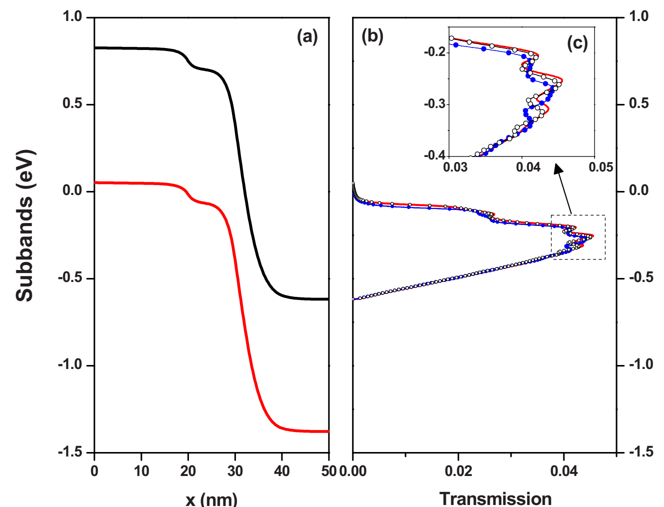

FIG. 4. (Color online) (a) A potential profile in a BTBT condition and (b) the corresponding transmission $T(E)$ as a function of energy E. (c) shows the magnified view as indicated in the figure. In (b) and (c), solid line represents $T(E)$ from using the full Hamiltonian and solid circles and open circles represent $T(E)$ from using the mode-space Hamiltonian with $N_M=144$ and 276, respectively.

Downloaded 19 Apr 2013 to 143.248.118.125. This article is copyrighted as indicated in the abstract. Reuse of AIP content is subject to the terms at: http://jap.aip.org/about/rights_and_permissions

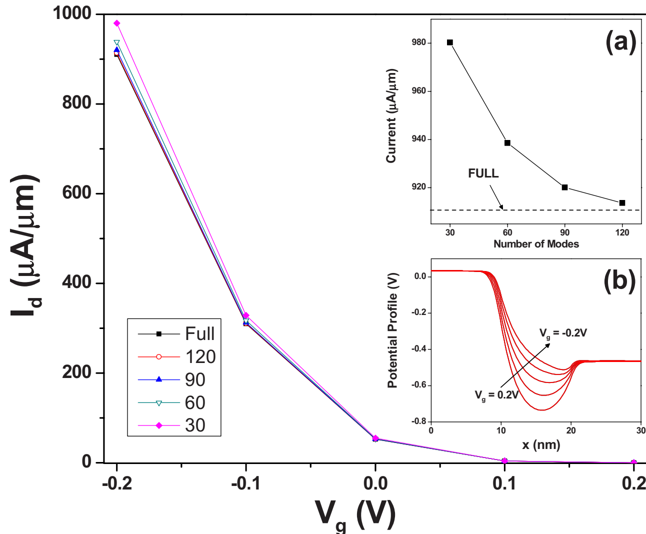

FIG. 5. (Color online) Self-consistent currents of a p-type Si nanowire with 5×5 nm^2 cross section and 10 nm channel length. Squares represent the current from using the full Hamiltonian and solid diamonds, open inverse triangles, solid triangles, and open circles represent currents from using the mode-space Hamiltonian with N_M=30, 60, 90, and 120, respectively. In (a), currents at V_g=−0.2 V calculated using the mode-space Hamiltonian as the number of modes is varied are shown. The current calculated using the full Hamiltonian represented by dashed line is shown as a guide to the eyes. In inset (b), the potential profile (along a line through the center of the nanowire cross-section) as the gate voltage is changed is shown.

tunnel FET whose conduction and valence band profiles are shown in the figure. The device is 20 nm long and has cross section of 5×5 nm^2, and its source and drain are p-doped and n-doped, respectively, with the doping density of 5×10^{19} cm^2. As can be seen in the figure, $T_{\mathrm{mode}}(E)$ of the mode-space Hamiltonian is already quite close to $T_{\mathrm{full}}(E)$ of full Hamiltonian when total 144 modes (24 modes for conduction band and 120 modes for valence band) are used for the mode-space Hamiltonian. When total 276 modes (36 modes for conduction band and 240 modes for valence band) are used, $T_{\mathrm{mode}}(E)$ nearly overlaps with $T_{\mathrm{full}}(E)$, and the tunneling current values, which can be obtained by integrating $T(E)$ after multiplying it with the difference of the source and drain Fermi functions, differ by a few tenth of 1%.

Finally, we compare the current-voltage characteristics self-consistently calculated from using the full and mode-space Hamiltonians, respectively. For this, we have used a 3×3 KP Hamiltonian without the spin-orbit (SO) coupling because with SO turned on (6×6 KP Hamiltonian), the full solution requires a huge amount of memories and very long simulation time. The SO-off model still captures all the coupling effects among different modes, so it can as well serve our purpose of benchmarking the mode-space solution with the full solution. Figure 5 shows the results for a Si p-type nanowire FET with 10 nm channel length and 5×5 nm^2 cross section. The drain voltage V_d=0.5 V and the gate voltage V_g is varied from 0.2 to −0.2 V. See inset (b) for the potential-profile change to the gate voltage. As can be seen in Fig. 5, the drain current $I_{\mathrm{mode}}(N_M)$ from using the mode-space Hamiltonian with number of mode N_M approaches the drain current I_{full} from using the full Hamiltonian as N_M is gradually increased and $I_{\mathrm{mode}}(120)$ almost overlaps with I_{full}.

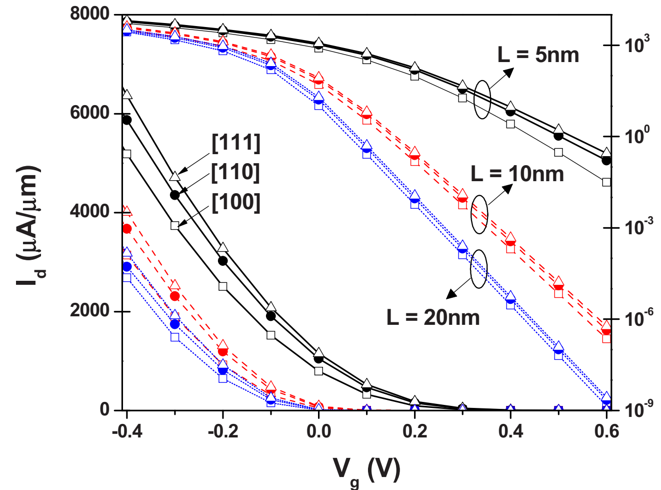

FIG. 6. (Color online) The current-voltage characteristics of a p-type Si nanowire of 5×5 cross section for three different orientations and three different channel lengths. Open squares, solid circles, and open triangles represent the [100], [110], and [111] directions, respectively, and solid lines, dashed lines, and dotted lines represent 5, 10, and 20 nm, respectively.

At V_g=−0.2 V, in particular, the relative errors of $I_{\mathrm{mode}}(N_M)$ with respect to I_{full} are around 7%, 3%, 1%, and 0.3% for N_M=30, 60, 90, and 120. See inset (a). Note that the currents in the figure were self-consistently calculated, starting with the same initial best-guessed potential at V_g=0.2 V and gradually increasing the gate voltage up to −0.2 V.

Having shown that our mode-space approach indeed works, with mode numbers ranging from 100 to 200 being sufficient to produce practically identical results to the full solution, we demonstrate in the next subsections the capability of our KP-based simulator by taking two important example systems, Si p-type nanowire FET and III-V nanowire tunnel FET.

B. Hole currents in Si nanowire *p*-FETs

We demonstrate in Fig. 6 simulation results for Si nanowire p-FETs with 5×5 nm^2 cross section. The 6×6 KP Hamiltonian with SO turned on was used. The source and drain are n-doped with density of 10^{20} cm^{-3}, the channel is intrinsic, the oxide thickness is assumed to be 1 nm, and the type of the gate is gate all around (GAA). Three channel lengths (5, 10, and 20 nm) and three transport directions ([100], [110], and [111]) were considered. In the long channel (20 nm) cases, the subthreshold slope (SS) for all the three orientations reaches the theoretical limit of 60 mV/decade. SS increases for shorter channel lengths, as expected. For L=10 nm, SS=68 mV/decade for all three directions, whereas for L=5 nm, SS=102, 122, and 129 mV/decade for the [100], [110], and [111] directions, respectively, which implies that the [100] direction is slightly less susceptible to the channel-length scaling than other two directions. The magnitude of the on currents are in the order $I_{111}>I_{110}>I_{100}$, which is consistent with the results in Ref. 17, although I_{111} and I_{110} are very close to each other for the same OFF current.

In Fig. 6, we can also find that the threshold voltage for shorter channel is shifted toward smaller (negatively) gate

Downloaded 19 Apr 2013 to 143.248.118.125. This article is copyrighted as indicated in the abstract. Reuse of AIP content is subject to the terms at: http://jap.aip.org/about/rights_and_permissions

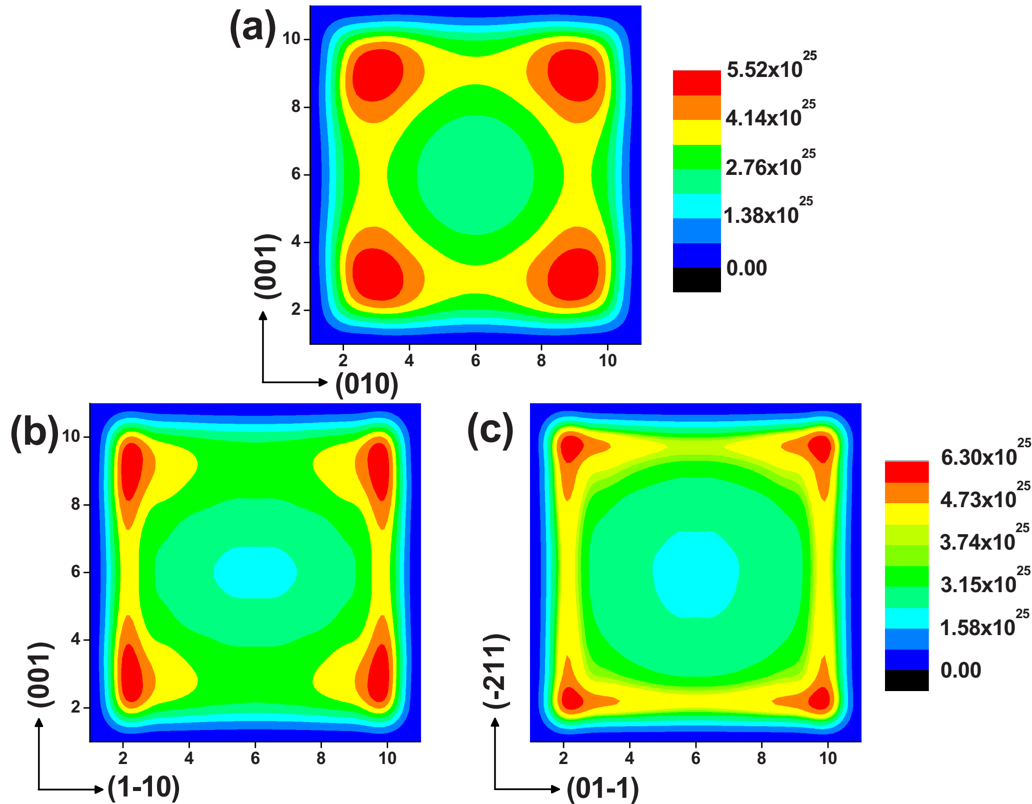

FIG. 7. (Color online) The charge distributions at the top of the barrier of a Si nanowire pMOSFET device with 10×10 nm^2 cross section and 40 nm channel length for the (a) [100], (b) [110], and (c) [111] Si orientations. The applied drain and gate voltages are 0.5 and −0.3 V, respectively, and the top of the barrier is located about 1 nm into the channel region from the channel/drain interface.

voltage, as in the case of n-type Si nanowire FETs.[18] For the [100] direction, for instance, the threshold voltage shifts for $L=10$ and 20 nm with respect to $L=20$ nm are 43 and 193 mV, respectively. After shifting the current curves such that the threshold voltages coincide, the on currents of the different channel lengths become almost the same, as they should be because of the assumed ballistic nature of the transport.

Our KP simulator is capable of simulating devices with relatively large cross section and long channel. Figure 7 shows the cross-sectional charge densities in p-type Si nanowire FETs with 10×10 nm^2 cross section and 40 nm channel length, for Si orientations [100], [110], and [111], respectively. Simulations were performed with SO turned off because SO plays a minor role in devices with relatively large cross sections. The charge densities were drawn at the top of the barrier in the On state (the gate voltage of −0.3 V was applied). The charge density distributions agree well with those by the top of the barrier model using the atomistic TB model.[17]

C. BTBT in III-V nanowire FETs

As an important application of our KP simulator, we now demonstrate BTBT in a p-i-n InAs nanowire tunnel FET. The 8×8 KP Hamiltonian was used in the simulation. The example device has the n-doped source and p-doped drain, each with doping density of 5×10^{19} cm^{-3}. The channel is intrinsic, the cross section is 5×5 nm^2, the oxide thickness is assumed to be 1 nm, and gates are GAA. The drain voltage of 0.3 V is applied. Figure 8(a) shows the BTBT currents for the three channel lengths, 5, 10, and 20 nm. SS for $L=20$ nm is about 20 mV/decade, which is much less than the 60 mV/decade limit of the conventional MOSFETs, but as the channel length is reduced, SS sharply increases; for $L=10$ nm, SS increases to about

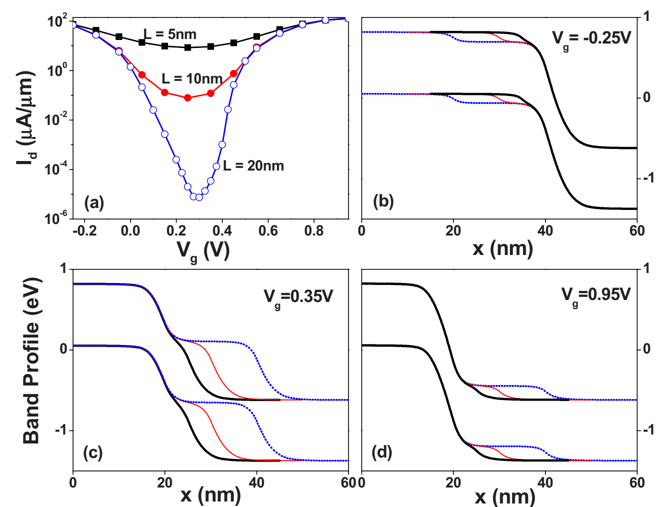

FIG. 8. (Color online) (a) The ambipolar currents due to the BTBT for $L=5$, 10, and 20 nm. (b), (c), and (d) are band profiles for $V_g=-0.25$, 0.35, and 0.95 V, respectively, where thick solid lines, thin solid lines, and dotted lines represent $L=5$, 10, and 20 nm, respectively. In (b), the band profiles for different channel lengths were shifted such that the drain contacts coincide with each other, whereas in (c) and (d), they were shifted such that source contacts coincide with each other.

Downloaded 19 Apr 2013 to 143.248.118.125. This article is copyrighted as indicated in the abstract. Reuse of AIP content is subject to the terms at: http://jap.aip.org/about/rights_and_permissions

90 mV/decade. In the insets (b) and (d) are shown BTBT conditions at the gate-bias voltages of −0.25 and 0.95 V, respectively, which correspond to the saturated state in the left and right branches, respectively. At V_g=−0.25 V, electrons near the conduction band edge tunnels into the valence band, whereas at V_g=0.95 V, holes near the valence band edge tunnels into the conduction band. As can be seen in the insets, the interband tunneling distances for the three different channel lengths are all the same, leading to the same saturation currents regardless of the channel length. At V_g =0.35 V where the current is minimum, the tunneling distance becomes shorter in proportion to the channel-length reduction, as shown in the inset (b), resulting in higher minimum currents and higher SS as well. Due to the asymmetry between the conduction and valence band, the ambipolar currents are not symmetrical around the current minimum. It is observed in the figure that the hole-tunneling branch gives rise to stiffer rise of currents.

IV. CONCLUSIONS

We have developed a practical, full-quantum nanowire FET simulator based on the eight-band KP theory and demonstrated its capability. We have shown detailed steps for construction of real-space, k-space, and mode-space KP Hamiltonians suitably discretized for transport simulation in 3D nanowires. In particular, we have elaborated on definition of the mode-space basis and systematic selection of modes. We have quite thoroughly examined the validity of our mode-space approach by comparing the results from using the mode-space Hamiltonian and from using the full Hamiltonian. We have found that, with number of modes ranging from 100 to 200, our mode-space approach faithfully reproduces solutions from full Hamiltonian. This, together with our efficient way to solve the cross-sectional eigenvalue problems, enabled us to develop highly efficient, practical full-quantum simulator that can treat both the conduction and valence bands. Our KP simulator has clear advantage over the TB based quantum transport simulators in terms of the size of the device that can be considered by the tool and the computational speed: the cross section of a p-type Si nanowire FET can be readily treated up to $10\times 10\ \text{nm}^2$ and a full current-voltage sweep for a typical-sized device can be finished within a few hours using a small cluster computer. The simulator described here will be uploaded to nanoHUB and open to public.[19]

ACKNOWLEDGMENTS

This research was supported by the Ministry of Knowledge Economy, Korea, under the ITRC support program supervised by the IITA (IITA-2009-C1090-0902-0014) and by the Network for Computational Nanotechnolgy of Purdue University.

APPENDIX A: *K·P* HAMILTONIAN

The 8×8 KP Hamiltonian is given by[20,21]

$$H_{\text{KP}}(k_x,k_y,k_z) = H_{0,\text{KP}}(k_x,k_y,k_z) + V_{\text{KP}}, \tag{A1}$$

where

$$H_{0,\text{KP}} = \begin{bmatrix} C & 0 & -P_+\sqrt{2} & 0 & \sqrt{2/3}P_z & P_-/\sqrt{6} & P_z/\sqrt{3} & P_-/\sqrt{3} \\ cc & C & 0 & P_-/\sqrt{2} & -P_+/\sqrt{6} & \sqrt{2/3}P_z & P_+/\sqrt{3} & -P_z/\sqrt{3} \\ cc & cc & -P-Q & 0 & S & -R & S/\sqrt{2} & -\sqrt{2}R \\ cc & cc & cc & -P-Q & -R^* & -S^* & \sqrt{2}R^* & S^*/\sqrt{2} \\ cc & cc & cc & cc & -P+Q & 0 & \sqrt{2}Q & -\sqrt{3/2}S \\ cc & cc & cc & cc & cc & -P+Q & -\sqrt{3/2}S^* & -\sqrt{2}Q \\ cc & cc & cc & cc & cc & cc & -P-\Delta_{\text{SO}} & 0 \\ cc & cc & cc & cc & cc & cc & cc & -P-\Delta_{\text{SO}} \end{bmatrix}, \tag{A2}$$

where

$$C = \frac{\hbar^2}{2m_0}\gamma_c(k_x^2 + k_y^2 + k_z^2), \tag{A3}$$

$$P = \frac{\hbar^2}{2m_0}\gamma_1(k_x^2 + k_y^2 + k_z^2), \tag{A4}$$

$$Q = \frac{\hbar^2}{2m_0}\gamma_2(k_x^2 + k_y^2 - 2k_z^2), \tag{A5}$$

$$R = -\frac{\hbar^2}{2m_0}\sqrt{3}\{\gamma_2(k_x^2 - k_y^2) - 2i\gamma_3 k_x k_y\}, \tag{A6}$$

$$S = \frac{\hbar^2}{2m_0}2\sqrt{3}\gamma_3(k_x - ik_y)k_z, \tag{A7}$$

$$P_\pm = P_0(k_x \pm ik_y), \tag{A8}$$

$$P_z = P_0 k_z, \tag{A9}$$

where

Downloaded 19 Apr 2013 to 143.248.118.125. This article is copyrighted as indicated in the abstract. Reuse of AIP content is subject to the terms at: http://jap.aip.org/about/rights_and_permissions

$$\gamma_c = \frac{1}{m_c^*} - \frac{E_P}{3}\left(\frac{2}{E_g} + \frac{1}{E_g+\Delta_{SO}}\right), \tag{A10}$$

$$\gamma_1 = \gamma_1^L - E_P/(3E_g + \Delta_{SO}), \tag{A11}$$

$$\gamma_2 = \gamma_2^L - E_P/(6E_g + 2\Delta_{SO}), \tag{A12}$$

$$\gamma_3 = \gamma_3^L - E_P/(6E_g + 2\Delta_{SO}), \tag{A13}$$

$$P_0 = \sqrt{E_P\hbar^2/2m_0}, \tag{A14}$$

where γ_i^L where $i=1,2,3$ are Luttinger parameters, Δ_{SO} is the SO splitting energy, E_g is the band gap, E_P is a band-mixing parameter, and m_c^* is the conduction band effective mass. In Eq. (A1),

$$V_{KP} = \begin{bmatrix} E_C I_{2\times2} & 0 \\ 0 & E_V I_{6\times6} \end{bmatrix}, \tag{A15}$$

where E_C and E_V are conduction and valence band edges, respectively, and $I_{n\times n}$ is an $n\times n$ identity matrix.

APPENDIX B: THE *K·P* HAMILTONIAN DISCRETIZED IN THE *K*-SPACE

The Hamiltonian $\mathcal{H}_R$ in Eq. (2) discretized in the real space can be transformed to k-space via a unitary transformation as follows:

$$\mathcal{H}_K = \mathcal{U}_K^\dagger \mathcal{H}_R \mathcal{U}_K, \tag{B1}$$

where

$$\mathcal{U}_K = \begin{bmatrix} U_K & & & & \\ & U_K & & & \\ & & U_K & & \\ & & & \ddots & \\ & & & & U_K \end{bmatrix}, \tag{B2}$$

where U_K is an unitary matrix which is a block matrix with blocks of size $N_b\times N_b$; its (M,L) block $[U_K]_{ML}$ is given by

$$[U_K]_{ML} = \frac{2}{\sqrt{N_y N_z}} \sin(\vec{k}_L, \vec{r}_M) I_{N_b\times N_b}, \tag{B3}$$

where

$$\sin(\vec{k}_L, \vec{r}_M) \equiv \sin(k_p y_m)\sin(k_q z_n) \tag{B4}$$

and

$$\vec{k}_L = \left(\frac{p\pi}{L_y}, \frac{q\pi}{L_z}\right) \tag{B5}$$

is the Lth grid point in the k-space (where $1\le p\le N_y$ and $1\le q\le N_z$) and L_y and L_z are device length in the y and z directions, respectively, and

$$\vec{r}_M = (y_m, z_n) \tag{B6}$$

is the Mth grid point in the real space (on the cross-sectional plane), where $M=(m-1)N_z+n$, where $1\le m\le N_y$ and $1\le n\le N_z$. $\mathcal{H}_K$ in Eq. (B1) can be written as in Eqs. (5)–(9).

The block (L,L') of H_{0K} in Eq. (8), where L and L' index the k-space grid points $(1\le L,L'\le N_yN_z)$, is an $N_b\times N_b$ matrix given by

$$[H_{0K}]_{LL'} = \frac{4}{N_yN_z}\sum_{M=1}^{N_yN_z}\sum_{M'=1}^{N_yN_z} \sin(\vec{k}_L,\vec{r}_M) \times [H_{0R}]_{MM'} \sin(\vec{k}_{L'},\vec{r}_{M'}), \tag{B7}$$

where $[H_{0R}]_{MM'}$ which is an $N_b\times N_b$ matrix is the element (M,M') of H_{0R} in Eq. (3), where M and M' index the real-space grid points.

To evaluate Eq. (B7) analytically, we take the limit where the real space mesh size goes to zero and $N_y,N_z\to\infty$. Alternatively, one can directly take the KP Hamiltonian in Eq. (A2) with k_x discretized in the real space as usual and $k_{y(z)}$ replaced by the operator $-i\partial/\partial y(z)$, multiply it with $2/\sqrt{L_yL_z}\sin(\vec{k}_L,\vec{r})$ to its left and with $2/\sqrt{L_yL_z}\sin(\vec{k}_{L'},\vec{r})$ to its right where $\vec{r}=(y,z)$, and integrate over y and z over the device region.

For $N_b=8$, the 8×8 matrix $[H_{0K}]_{LL'}$ has the same elements as the 8×8 matrix $H_{0,KP}$ in Eq. (A2) but C, P, Q, etc are replaced as follows:

$$C_{LL'} = \frac{\hbar^2}{2m_0}\gamma_c\left[\frac{2}{(\Delta x)^2} + k_p^2 + k_q^2\right]\delta_{p,p'}\delta_{q,q'}, \tag{B8}$$

$$P_{LL'} = \frac{\hbar^2}{2m_0}\gamma_1\left[\frac{2}{(\Delta x)^2} + k_p^2 + k_q^2\right]\delta_{p,p'}\delta_{q,q'}, \tag{B9}$$

$$Q_{LL'} = \frac{\hbar^2}{2m_0}\gamma_2\left[\frac{2}{(\Delta x)^2} + k_p^2 - 2k_q^2\right]\delta_{p,p'}\delta_{q,q'}, \tag{B10}$$

$$R_{LL'} = -\frac{\hbar^2}{2m_0}\sqrt{3}\gamma_2\left[\frac{2}{(\Delta x)^2} - k_p^2\right]\delta_{p,p'}\delta_{q,q'}, \tag{B11}$$

$$S_{LL'} = i\frac{\hbar^2}{2m_0}2\sqrt{3}\gamma_3\left(\frac{4k_{p'}}{\pi}\frac{p}{p^2-p'^2}\delta_{p+p',\mathrm{odd}}\right) \times \left(\frac{4k_{q'}}{\pi}\frac{q}{q^2-q'^2}\delta_{q+q',\mathrm{odd}}\right), \tag{B12}$$

$$[P_\pm]_{LL'} = \pm P_0\left(\frac{4k_{p'}}{\pi}\frac{p}{p^2-p'^2}\delta_{p+p',\mathrm{odd}}\right), \tag{B13}$$

$$[P_z]_{LL'} = -iP_0\left(\frac{4k_{q'}}{\pi}\frac{q}{q^2-q'^2}\delta_{q+q',\mathrm{odd}}\right), \tag{B14}$$

where Δx is the grid spacing in the transport direction, where (p,q) and (p',q') are the coordinates of the k-space grid points L and L', respectively, as given by Eq. (B5). In the above equation, $\delta_{p+p',\mathrm{odd}}$ means that the value is 1 if $p+p'$ is an odd integer or 0 otherwise.

The element $[W_K]_{LL'}$ of W_K in Eq. (7) can be evaluated similarly and has the following terms:

$$C_{LL'} = -\frac{\hbar^2}{2m_0}\gamma_c\frac{1}{(\Delta x)^2}\delta_{p,p'}\delta_{q,q'}, \tag{B15}$$

Downloaded 19 Apr 2013 to 143.248.118.125. This article is copyrighted as indicated in the abstract. Reuse of AIP content is subject to the terms at: http://jap.aip.org/about/rights_and_permissions

$$P_{LL'} = -\frac{\hbar^2}{2m_0}\gamma_1\frac{1}{(\Delta x)^2}\delta_{p,p'}\delta_{q,q'}, \tag{B16}$$

$$Q_{LL'} = -\frac{\hbar^2}{2m_0}\gamma_2\frac{1}{(\Delta x)^2}\delta_{p,p'}\delta_{q,q'}, \tag{B17}$$

$$R_{LL'} = \frac{\hbar^2}{2m_0}\left\{\sqrt{3}\gamma_2\frac{1}{(\Delta x)^2}\delta_{p,p'} - i2\sqrt{3}\gamma_3\frac{1}{2\Delta x}\frac{4k_{p'}}{\pi}\frac{p}{p^2-p'^2}\delta_{p+p',\mathrm{odd}}\right\}\delta_{q,q'}, \tag{B18}$$

$$S_{LL'} = -\frac{\hbar^2}{2m_0}2\sqrt{3}\gamma_3\frac{1}{2\Delta x}\left(\frac{4k_{q'}}{\pi}\frac{q}{q^2-q'^2}\delta_{q+q',\mathrm{odd}}\right)\delta_{p,p'}, \tag{B19}$$

$$[P_\pm]_{LL'} = \mp iP_0\frac{1}{2\Delta x}\delta_{p,p'}\delta_{q,q'}, \tag{B20}$$

$$[P_z]_{LL'} = 0. \tag{B21}$$

An extra care should be taken for conjugates of $P_\pm$ and P_z in the discretized matrix. For instance, in $[W_K]_{LL'}$,

$$[P_\pm^\dagger]_{LL'} = [P_\pm]_{LL'} = \mp iP_0\frac{1}{2\Delta x}\delta_{p,p'}\delta_{q,q'}, \tag{B22}$$

which stems from the fact that $k_x^\dagger = k_x$ or $[-i(\partial/\partial_x)]^\dagger = -i(\partial/\partial_x)$.

To numerically evaluate $V_K(i)$ in Eq. (9), one can either use a fast Fourier transform (FFT) for an uniform y-z grid or directly multiply the matrices for a nonuniform grid. For the latter, the prefactor of $[U_K]_{ML}$ in Eq. (B3) should be replaced with

$$\frac{2}{\sqrt{N_yN_z}} \rightarrow \frac{2}{\sqrt{L_yL_z}}\sqrt{\Delta y_m}\sqrt{\Delta z_n}, \tag{B23}$$

where Δy_m and Δz_n are grid spacing at y_m and z_n, respectively. If one judiciously use a matrix multiplication routine such as the one provided in LAPACK and optimized for a given computer platform, a fast computation, compatible with the speed of FFT, can be achieved.

APPENDIX C: SIZE REDUCTION OF *K*-SPACE HAMILTONIAN

When constructing the k-space Hamiltonian matrices in Eqs. (6) and (7), a simple scheme to index grid points in the k-space would be such that index L simply increases as

$$L = L(p,q) = (p-1)N_z + q, \tag{C1}$$

where $1 \leq q \leq N_z$ and $1 \leq p \leq N_y$ as before. In this work, we have chosen a different indexing scheme as follows. We evaluate the magnitude $|\vec{k}_L|$ at each k-space grid point L,

$$|\vec{k}_L|^2 = \left(\frac{p\pi}{L_y}\right)^2 + \left(\frac{q\pi}{L_z}\right)^2, \tag{C2}$$

and reorder index L such that $|\vec{k}_L|^2$ is in the increasing order. The simple indexing scheme corresponds to moving row by row in the k-space, while our scheme corresponds to covering grid points such that the distance from the origin gradually increases, as illustrated in Fig. 9.

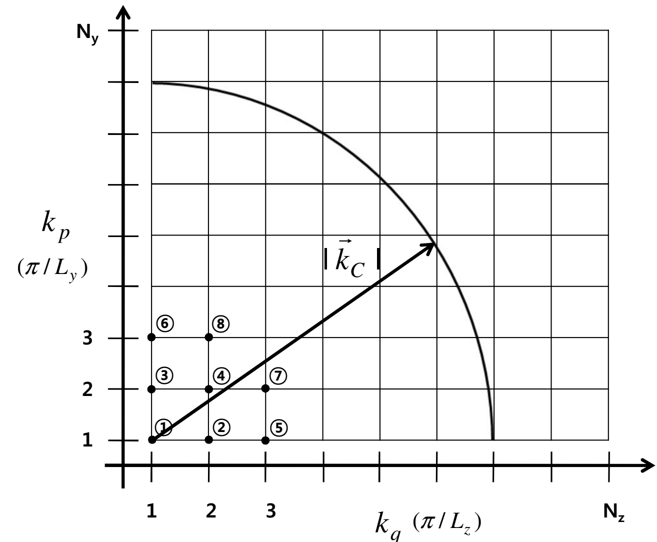

FIG. 9. The scheme to index k-space grid points. We define $k_p = p\pi/L_y$ and $k_q = q\pi/L_z$, and index grid points in the increasing order of the magnitude $k_p^2 + k_q^2$ as indicated by the circled numbers.

We draw a vector in the k-space whose magnitude is $|\vec{k}_C|$ as shown in Fig. 9 and denote by N_K the number of the grid points whose, distance from the origin is smaller than $|\vec{k}_C|$. Instead of using the total N_yN_z grid points, we select to use smaller N_K grid points, i.e., $1 \leq L \leq N_K$. Then the sizes of the k-space matrices in Eqs. (6) and (7) become $N_bN_K \times N_bN_K$ instead of $N_bN_yN_z \times N_bN_yN_z$.

[1] Y. Cui, Z. Zhong, D. Wang, W. Wang, and M. Lieber, Nano Lett. **3**, 149 (2003).
[2] H.-S. Philip Wong, Solid-State Electron. **49**, 755 (2005).
[3] J. Wang, E. Polizzi, and M. Lundstrom, J. Appl. Phys. **96**, 2192 (2004).
[4] M. Bescond, K. Nehari, J. L. Autran, N. Cavassilas, D. Munteanu, and M. Lannoo, Tech. Dig. - Int. Electron Devices Meet. **2004**, 617.
[5] M. Shin, IEEE Trans. Nanotechnol. **6**, 230 (2007).
[6] J. Wang, A. Rahman, A. Ghosh, G. Klimeck, and M. Lundstrom, IEEE Trans. Electron Devices **52**, 1589 (2005).
[7] K. Nehari, N. Cavassilas, J. L. Autran, M. Bescond, D. Munteanu, and M. Lannoo, Proceedings of the 35th European Solid-State Device Research Conference, 2005 (ESSDERC, 2005), 12–16 September 2005 (unpublished), pp. 229–232.
[8] E. Kane, J. Phys. Chem. Solids **1**, 82 (1956).
[9] Y. X. Liu, D. Z.-Y. Ting, and T. C. McGill, Phys. Rev. B **54**, 5675 (1996).
[10] D. Mamaluy, D. Vasileska, M. Sabathil, T. Zibold, and P. Vogl, Phys. Rev. B **71**, 245321 (2005).
[11] H. Minari and N. Mori, J. Comput. Electron. **7**, 293 (2008).
[12] M. Luisier, A. Schenk, W. Fichtner, and G. Klimeck, Phys. Rev. B **74**, 205323 (2006).
[13] M. Shin, J. Appl. Phys. **101**, 024510 (2007).
[14] G. Fiori, G. Iannaccone, and G. Klimeck, IEEE Trans. Nanotechnol. **6**, 475 (2007).
[15] R. Lake, G. Klimeck, R. C. Bowen, and D. Jovanovic, J. Appl. Phys. **81**, 7845 (1997).
[16] C. Rivas and R. Lake, Phys. Status Solidi B **239**, 94 (2003).
[17] N. Neophytou, A. Paul, and G. Klimeck, IEEE Trans. Nanotechnol. **7**, 710 (2008).
[18] M. Shin, IEEE Trans. Electron Devices **55**, 737 (2008).
[19] KPnanoFET on nanoHUB.org. Available at https://www.nanohub.org/tools/kpnanofet
[20] M. El kurdi, G. Fishman, S. Sauvage, and P. Boucaud, Phys. Rev. B **68**, 165333 (2003).
[21] T. B. Bahder, Phys. Rev. B **41**, 11992 (1990).

Downloaded 19 Apr 2013 to 143.248.118.125. This article is copyrighted as indicated in the abstract. Reuse of AIP content is subject to the terms at: http://jap.aip.org/about/rights_and_permissions